Ru- and Ir-complexes decorated periodic mesoporous organosilicas as sensitizers for artificial photosynthesis

Raúl Rojas-Luna,[a] Miguel Castillo-Rodríguez,[b] José R. Ruiz,[a] César Jiménez-Sanchidrián,[a] Dolores Esquivel[a*] and Francisco J. Romero-Salguero[a*]

[a]Departamento de Química Orgánica, Instituto Químico para la Energía y el Medioambiente (IQUEMA), Facultad de Ciencias, Universidad de Córdoba, Campus de Rabanales, 14071 Córdoba, Spain.

[b]Departamento de Física Aplicada, Radiología y Medicina Física, Universidad de Córdoba, Campus de Rabanales, 14071 Córdoba, Spain

* q12esmem@uco.es (D.E.); qo2rosaf@uco.es (F.J.R.-S.)

Abstract

A versatile and facile strategy based on an inverse demand Diels-Alder reaction between 5-norbornen-2-yltriethoxysilane and a tetrazine derivative has been established for the synthesis of a new triethoxysilane precursor containing dipyridylpyridazine units. Such precursor has been incorporated into the mesostructure of an ethylene-bridged periodic mesoporous organosilica (PMO) through a one-pot synthesis via co-condensation method. Upon attachment of Ru- and Ir-complexes to the pendant N-chelating heterocyclic ligands, the resulting decorated PMO have acted as photosensitizers in artificial photosynthesis systems. The deposition of Pt on these PMO has allowed to obtain efficient photocatalytic materials for the hydrogen evolution reaction as a result of electron transfer from the light harvesting Ru- and Ir-complexes to the supported Pt nanoparticles through methyl viologen as electron relay. They have exhibited total turnover number values of 553 and 846, respectively, under visible light irradiation. The role played by each component and the stability of the photocatalytic systems have been discussed. The present approach paves the way to the synthesis of different materials with coordination sites capable of forming surface complexes to be applied as sensitizers and catalysts.

Keywords: Inverse demand Diels-Alder reaction, dipyridylpyridazine units, periodic mesoporous organosilicas, Ru- and Ir-photosensitizers, artificial photosynthesis, hydrogen evolution reaction

1. Introduction

N-chelating ligands have attracted a great interest in coordination chemistry due to their rich complexation ability towards transitions metal ions, yielding organometallic systems of great relevance in many catalytic applications[1]. In this field, 1,2,4,5-tetrazine and its corresponding 3,6-disubstituted derivatives, characterized by electron and charge transfer phenomena and by the ability to complex one or two metal centers due to their multiple metal binding sites, represent one of the most studied ligand systems[2,3]. They are able to provide a wide variety of applications such as the formation of transitions metal mononuclear[4–6], dinuclear[7–9] and polinuclear[10–12] complexes, biorthogonal chemistry[13,14] and as building blocks in supramolecular systems[2,15,16]. Moreover, tetrazine derivatives act as excellent starting materials for the synthesis of pyridazine derivatives through an inverse electron demand Diels-Alder reaction (iEDDA)[17,18].

In recent decades, iEDDA reactions have positioned as a novel 'click chemistry' strategy in which two components react under mild conditions with high selectivity, high yield, and few or inoffensive byproducts[19,20]. Electron-poor dienes such as tetrazines and electron-rich dienophiles like trans-cyclooctene, norbornene, and cyclopropene derivatives react via an inverse electron demand Diels-Alder reaction leading to 1,4-dihydropyridazines as a metal-free click reaction[21]. Norbornenes stand out due to their straightforward synthesis, their stability, and their relatively small molecular size[21]. Among the reported norbornene derivatives, those containing alkoxysilane groups have attracted a great interest in the polymer industry as promising silyl agents to produce a variety of polymeric composite materials[22–26]. Although siloxane norbornenes have been prepared by olefin hydrosilylation of 2,5-norbornadienes[27], currently the most promising strategy to obtain them is through Diels-Alder reaction between a vinyltrialkoxysilane and dicyclopentadiene[28]. As previously mentioned, iEDDA reactions between norbornene and tetrazine derivatives lead to interesting N-chelating ligands for the coordination of a wide variety of transition metals.

The heterogenization of organometallic complexes is highly attractive in virtue of their potential applications, particularly as catalysts. Thus, transition metal-bipyridine complexes have been incorporated in the channels of porous materials using several approaches. First attempts were focused on the adsorption of *bis*- and *tris*(bipyridine) Fe^{+2}, Mn^{+2} or Ru^{+2} complexes into the channels of mesoporous silica or aluminosilica

materials via ion exchange or incipient-wetness impregnation[29–33]. Later, the use of silane coupling agents led to the formation of metal bipyridine complexes tethered covalently on the surface of mesoporous silicas[34,35]. Although initially these studies were addressed to immobilize metal-bipyridine complexes on solid supports to be used on common heterogenous catalytic processes, further on the interest was extended to exploit the luminescent properties of photoactive lanthanide and ruthenium complexes for optical devices[36–38]. In all these cases, the organosilane precursors possessed relatively long and/or flexible alkyl chains, so that they could only be incorporated in fairly small amounts into the synthesis medium.

Numerous ongoing efforts are driven to produce hydrogen by photocatalytic water splitting.. One of the most important challenges on photocatalytic hydrogen evolution systems is the choice of a high-performance photosensitizer with a broad light adsorption range, a high molar extinction coefficient, a suitable redox potential for electron transfer, a long excited states lifetime for effective charge separation and a long-term stability.[39] Many different types of chromophores have been used as light harvesters since the first photocatalytic water splitting system reported[40]. Metal-free organic dyes such as rose Bengal, fluorescein or Eosin Y, and metal complexes such as $[Ru(bpy)_3]^{2+}$ or $[Ir(bpy)(ppy)_2]^{+}$ have been widely studied for hydrogen evolution reaction (HER) during last decades. Although the former ones are less expensive than the latter, they are characterized by short lifetimes and, consequently, suffer a quick deactivation. Otherwise noble-metal complexes photosensitizers show higher stability due to the strong coupling effects between metals and their ligands[41]. Among them, two of the most widely studied metal complexes as photosensitizers are $[Ru(bpy)_3]^{+2}$, due to its strong visible light absorption and long excited state lifetimes, and Ir^{+3} complexes with higher photostability and improved luminescent properties compared to the previous ones. Despite these photosensitizers have been a subject of study in multitude of homogeneous catalytic systems for light-driven hydrogen production, recent approaches are being addressed for the incorporation of such photoactive complexes into highly porous frameworks, such as MOFs[42,43], PMOs[44] and, more recently, COFs[45].

Wang et col.[43] developed the first MOF-based photocatalyst through the loading of Pt nanoparticles into the cavities of a MOF built from $[Ir^{III}(ppy)_2(bpy)]$ linkers.. More recently, both functional components – photosensitizer and proton reduction catalyst – were successfully incorporated into MOF framework with two different transition metal

complexes, $[Ru(dcbpy)(bpy)_2]^{+2}$ and $Pt(dcbpy)Cl_2$, respectively. The proximity between both components grafted on the pore surface allowed a facile electron transfer from the Ru to the Pt-catalyst[42]. Concerning PMO, Inagaki et col.[44] accomplished the first and, to the best of our knowledge, the unique example of a H_2 production photocatalytic system integrating a $Ru(bpy)_3^{+2}$ complex embedded in the pore walls and platinum on the pore surface as photosensitizer and catalyst, respectively. It involved the previous synthesis of a PMO containing 2,2'-bipyridine ligands, which acts as a solid chelating ligand capable of forming different metal transition complexes, including those of iridium, ruthenium, rhenium, and palladium.

Despite the different intrinsic properties of each porous frameworks, all of them provide versatile and novel platforms to integrate different functional components for the synthesis of efficient solar energy conversion systems. In this sense, the incorporation of both components – photosensitizer and catalyst – into the same material enables synergistic functions for efficient hydrogen evolution reaction. Herein, we report for the first time the synthesis of a novel heterocyclic bipyridine-like triethoxysilane precursor (Ndppz) through iEDDA reaction between 5-norbornen-2-yltriethoxysilane and a tetrazine derivative, 3,6-di-(2-pyridyl)-1,2,4,5-tetrazine, which allows the integration of dipyridilpyridazine moieties within the pore of a periodic mesoporous organosilica (PMO). PMO are particularly stable to be used under aqueous conditions due to their hydrophobic nature[46]. In this case, the incorporation of this novel precursor in the mesostructure using a one-pot synthesis via co-condensation method provides these materials with a high coordination ability. Specifically, artificial photosynthesis systems based on PMO have been prepared through the formation of surface Ru- and Ir-complexes as photosensitizers and Pt as catalyst and tested for the HER under visible irradiation.

2. Experimental Section

Synthesis of the organosilane precursor (Ndppz)

Prior to the synthesis of the precursor, the tetrazine derivative, 3,6-di-(2-pyridyl)-1,2,4,5-tetrazine, was prepared following a procedure already reported by our research group[47,48]. This organic compound was further used as diene in the Diels-Alder reaction with 5-(bicycloheptenyl)triethoxysilane according to the procedure reported by Blackman et al.[18] Typically, a two-neck round-bottom flask was charged with a solution of 3,6-di-(2-pyridyl)-1,2,4,5-tetrazine (0.3 g, 1.3 mmol) in anhydrous THF (13 mL) under N_2 atmosphere. Then, 5-(bicycloheptenyl)triethoxysilane (0.56 mL, 2.1 mmol) was added to the solution and the mixture was stirred at room temperature for 30 min. After that, the purple solution turned orange, indicating that the reaction had gone to completion. Subsequently, a solution of DDQ (0.3 g, 1.3 mmol) in anhydrous THF (5 mL) was added to the mixture under stirring at room temperature. The solvent was completely removed using a rotary evaporator, and the resulting residue was purified by chromatography on silica gel (eluent: hexane/ethyl acetate = 1:0 to 1:1) to give **Ndppz** (325 mg, 54%) as a white solid (Scheme 1). ^{1}H NMR (300 MHz, $CDCl_3$) δ 8.75 (ddd, J = 4.8, 1.8, 0.9 Hz, 1H), 8.69 (ddd, J = 4.8, 1.8, 0.9 Hz, 1H), 8.57 (dt, J = 2.3, 1.1 Hz, 1H), 8.54 (dt, J = 2.3, 1.0 Hz, 1H), 7.87 (dddd, J = 8.2, 7.5, 1.8, 0.7 Hz, 2H), 7.34 (dddd, J = 7.4, 4.8, 2.4, 1.2 Hz, 2H), 4.60 – 4.48 (m, 2H), 3.91 (qd, J = 7.0, 0.7 Hz, 6H), 2.31 (ddd, J = 11.9, 6.3, 4.1 Hz, 1H), 1.92 (dt, J = 9.4, 1.4 Hz, 1H), 1.65 (dt, J = 9.4, 2.0 Hz, 1H), 1.51 (ddd, J = 11.9, 9.9, 2.1 Hz, 1H), 1.24 (t, J = 7.0 Hz, 9H), 0.92 – 0.77 (m, 1H) (Fig. S1). ^{13}C NMR (300 MHz, $CDCl_3$,) δ 156.2, 152.7, 151.2, 149.9, 149.3, 149.1, 147.3, 136.9, 123.8, 123.2, 58.9, 47.0, 43.4, 43.0, 27.3, 20.7, 18.6 (Fig. S2).

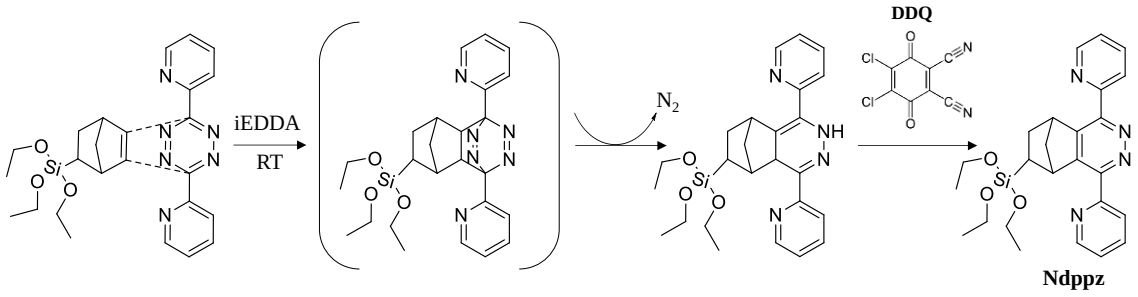

Scheme 1. Synthesis of Ndppz through Diels-Alder reaction of the tetrazine derivative with 5-(bicyloheptenyl)triethoxysilane.

Synthesis of NdppzPMO

Periodic mesoporous organosilica was synthesized according to the procedure reported by Inagaki et al.[49] for the synthesis of phenylpyridine-bridged PMO with some modifications. Typically, a mixture of organosilane precursors (2.04 mmol) with a molar ratio of 70 % 1,2-bis(triethoxysilyl)ethane and 30 % Ndppz in ethanol (15 mL) was added dropwise under vigorous stirring to a clear solution of octadecyltrimethylammonium bromide (OTAB, 0.96 g) and distilled water (53 mL) in basic media (6 M NaOH, 0.89 mL). The mixture was stirred at room temperature for 24 h, and further aged at 97 ºC for 6 days under static conditions. The resulting material was collected by filtration, washed thoroughly with water and dried under vacuum. To remove the surfactant, 1 g of as-synthesized material was refluxed in 50 mL of ethanol and 1 mL of concentrated HCl for 24 h. After repeating this extraction process twice, the material was recovered by filtration, washed with acetone, and dried under vacuum at 90 ºC to give **NdppzPMO** as a pale pink powder (see Scheme 2).

Synthesis of Ru@NdppzPMO

A 100 mL round-bottom flask was charged with NdppzPMO (300 mg), $Ru(bpy)_2Cl_2 \cdot 3H_2O$ (40 mg, 0.076 mmol) and 60 mL of dry ethanol[50]. The resulting mixture was stirred and heated to reflux overnight. Afterwards, the solid was collected by filtration and washed several times with dichloromethane to guarantee the complete removal of any physisorbed metal complex. Finally, the material was dried under vacuum at 90 ºC to give **Ru@NdppzPMO** as an orange powder.

Synthesis of Ir@NdppzPMO

A 100 mL round-bottom flask was charged with Ndppz-PMO (200 mg), $[Ir(ppy)_2Cl]_2$ (22 mg, 0.041 mmol) and 50 mL of dichloromethane[51]. The reaction mixture was stirred at 45 ºC overnight. The solid was recovered by filtration and washed several times with dichloromethane to remove any unreacted iridium complex. Finally, the material was dried under vacuum at 90 ºC to give **Ir@NdppzPMO** as a pale orange powder.

Synthesis of Pt/M@NdppzPMO (M = Ru or Ir)

A 50 ml round-bottom flask was charged with M@NdppzPMO (100 mg), K_2PtCl_6 (64 mg, 0.15 mmol) and degassed distilled water (24 mL). The reaction mixture was stirred at 80 ºC for 24 h. Then, the material was recovered by filtration and washed with ethanol to remove any unreacted K_2PtCl_6. The resulting material, Pt/M@NdppzPMO, was obtained as a brown powder.

Photocatalytic hydrogen production

The photocatalytic hydrogen evolution tests were carried out using a headspace screw-thread vial. For it, Pt/Ru@NdppzPMO or Pt/Ir@NdppzPMO (1 mg) was dispersed in 10 mL of an aqueous acetate buffer solution (pH 5.0, 1 M) containing EDTA (20 mM) and MV (5 mM). The reaction vessel was sealed, and deoxygenated by bubbling N_2 into the solution for 10 min. Then, the vessel was placed in a Penn PhD Photoreactor M2 and irradiated with visible light (450 nm). Sample aliquots were taken at different time intervals using a gas-tight syringe and quantified by gas chromatography (Shimadzu GC-2010 Plus) equipped with a ShinCarbon ST column (2 m × 2 mm i.d.) and a barrier discharge ionization detector (BID).

After the reaction, the photocatalyst was filtered-off, washed with EtOH and CH_2Cl_2 and dried under vacuum. The photocatalyst was then reused without further purification under the same reaction conditions.

The catalytic activity was expressed as turnover number (TON), i.e., mol H_2 produced per mol of sensitizer (Ru or Ir) and, in order to take into account the degradation of the catalytic system, the total turnover number (TTN) was calculated as the mol H_2 produced per mol of sensitizer (Ru or Ir) during the catalyst lifetime.

3. Results and discussion

Synthetic strategy and characterization of a novel PMO containing dipyridylpyridazine moieties. As for the preparation of functionalized materials, the incorporation of dipyridylpyridazine ligands on the surface of different materials has been the subject of intensive research by our group during the last years[48,52–55]. Thus, based on

a hetero Diels-Alder reaction, the surface of mesoporous materials containing double bonds either vinyl-silica or ethenylene-bridged PMO was successfully post-functionalized by reaction with a tetrazine derivative, specifically 3,6-di(2-pyridyl)-1,2,4,5-tetrazine. Despite this synthetic approach allowed decorating the surface of the materials with N-chelating heterocyclic compounds, while preserving their mesoporous ordering, there were some drawbacks associated to the post-functionalization processes of solid supports by a Diels-Alder reaction. This reaction required high temperatures (> 150 ºC, but usually 200 ºC) and long reaction times (several days)[54,56,57]. On the other hand, the resulting materials were characterized by smaller surface areas and pore volumes than the parent materials, and relatively low loadings of the N-containing chelating groups (Table S1). In addition, the cleavage of C-Si bonds in PMO was observed in some cases, although in a small fraction (<15%)[56].

The incorporation of dipyridylpyridazine units using new trialkoxysilane precursors bearing this heterocyclic system would be highly interesting. Thus, a versatile strategy to synthesize such precursors has been developed here based on an efficient iEDDA reaction between the double bond of 5-(bicycloheptenyl)triethoxysilane and 3,6-di(2-pyridyl)-1,2,4,5-tetrazine, giving precursor Ndppz (Scheme 1). This precursor can be introduced in different materials by grafting or co-condensation procedures, therefore avoiding post-functionalization reactions. In this work, NdppzPMO material was synthesized by co-condensation of Ndppz precursor (30 mol%) and 1,2-bis(triethoxysilyl)ethane (70 mol%) in the presence of OTAB (octadecyltrimethylammonium bromide) as structure-directing agent under basic conditions (Scheme 2). After surfactant removal, a highly ordered ethylene-bridged PMO with pendant dipyridylpyridazine groups in the channels pores, which can act as attachment point to bind metallic complexes, was successfully achieved.

The amount of nitrogen in different batches of NdppzPMO determined by elemental analysis was between 0.36 – 0.39 mmol g^{-1}, which involves a loading of dipyridylpyridazine units close to 0.1 mmol g^{-1}. These results improve the loading of nitrogen with respect to the post-functionalization processes of tetrazine derivatives on analogous mesoporous supports previously reported by our research group, in which the amounts of nitrogen incorporated were 66% lower for dppz-vSilica material and 50% lower for the dppz-ePMO and dppz-vPMO materials (Table S1).

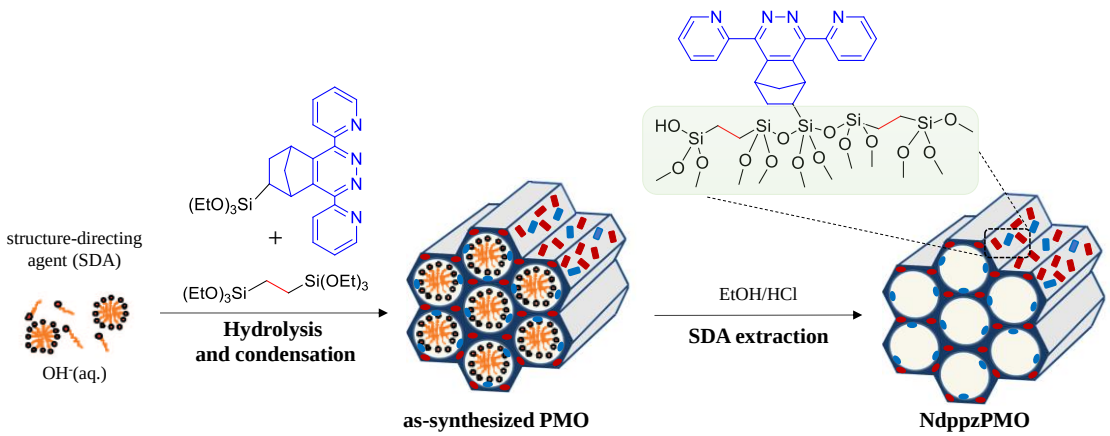

Scheme 2. Synthesis procedure of NdppzPMO.

X-ray diffraction pattern of NdppzPMO showed an intense peak at 2θ = 1.90º and two additional weak peaks at higher incidence angles, corresponding to the reflections (100), (110) and (200) of materials with 2D-hexagonal (*p6mm*) mesostructures[49] (Fig. 1a). Noteworthy, the high content of Ndppz (30 mol%) in the reaction mixture, despite its bulkiness, did not disturb the sol-gel process leading to well-ordered products[58].

NdppzPMO exhibited type-IV isotherms with a condensation step at a relative pressure around of 0.1 - 0.3, typical of ordered mesoporous materials (Fig. 1b). The average pore diameter and narrow pore size distribution of the material confirmed pores in the meso-range (Fig. 1b-inset). Physical properties of the material are listed in Table 1. The BET surface area (S_{BET}), pore volume (V) and pore diameter (D) were 917 m^2 g^{-1}, 0.42 cm^3 g^{-1} and 3.2 nm, respectively.

In addition to XRD and N_2 sorption measurements, TEM images corroborated the structural ordering of the synthesized material (Fig. S3).

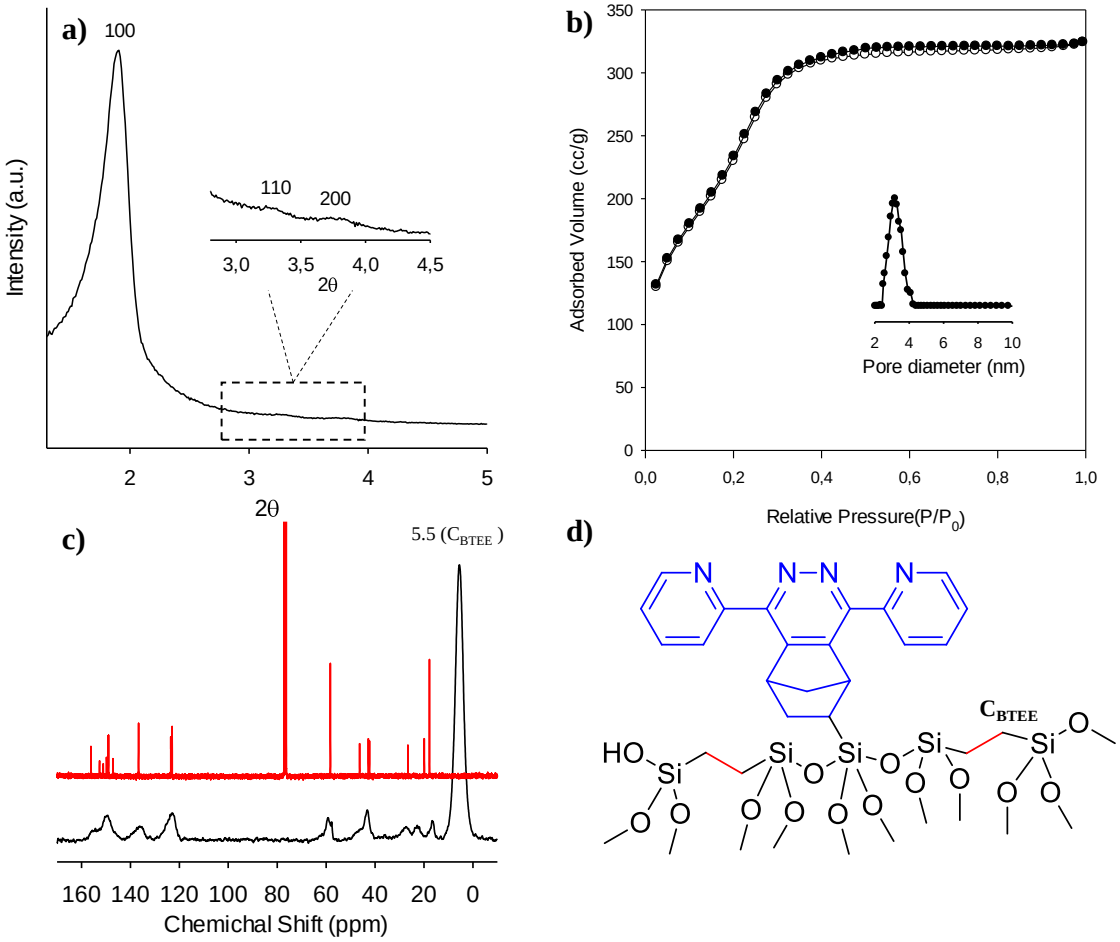

Fig. 1. Characterization of NdppzPMO. (a) X-ray diffraction pattern. (b) N_2 adsorption-desorption isotherms and pore size distribution (inset). (c) ^{13}C CP/MAS NMR spectrum of NdppzPMO (black solid line) and ^{13}C NMR spectrum of Ndppz precursor (red solid line). (d) Chemical structure of NdppzPMO.

Table 1. Physical properties of the NdppzPMO-based materials.

Material	a_0[a] (nm)	S_{BET} ($m^2\ g^{-1}$)	V[b] ($cm^3\ g^{-1}$)	D[b] (nm)	t[c] (nm)
NdppzPMO	5.3	917	0.42	3.2	2.1
Ru@NdppzPMO	5.3	695	0.31	2.6	2.7
Ir@NdppzPMO	5.3	789	0.37	2.8	2.5

[a]Estimated unit cell parameter assuming a 2D-hexagonal mesostructure**;** [b]Calculated from DFT-analysis; [c]Pore wall thickness calculated from (a_0 − D)

Solid-state ^{13}C CP/MAS NMR and Raman measurements revealed the presence of both organic silane precursors into the silica framework. The solid-state ^{13}C CP/MAS NMR spectrum of NdppzPMO (Fig. 1c) exhibited an intense signal at 5 ppm corresponding to ethylene carbons of the BTEE precursor[52,59]. Additional downfield (123, 126 and 150 ppm) and upfield (20-50 ppm) resonances were attributed to the Csp^2 of the pyridine and pyridazine groups, and to the Csp^3 of the norbornene group from the Ndppz precursor. These chemical shifts were similar to those of the Ndppz precursor (the assignment of individual carbons is described in detail in Fig. S2), thus confirming that such silane precursor remained intact on the mesostructure when the SDA was removed from the pores. Signals at 18 and 59 ppm were attributed to non-hydrolyzed ethoxy ($-OCH_2CH_3$) groups of the silane precursors. The absence of signals characteristic of the OTAB surfactant residues confirmed its complete removal.

Raman spectrum of Ndppz precursor (Fig. S4) showed several signals at 3067 and 3021 cm^{-1}, corresponding to =C-H stretching vibrations of the dipyridylpiridazine units. The intense peak at 1592 cm^{-1} was attributed to C=N vibration mode while signals at 1555, 1470 and 1445 cm^{-1} were characteristic of skeletal vibrations of N-heterocyclic components[54]. Si-O stretching mode was confirmed by the appearance of a peak at 993 cm^{-1}. Raman spectrum of NdppzPMO showed the same vibrational modes, but additionally several intense peaks around 2900 cm^{-1}, which were associated to the C-H stretching vibrations of the ethylene bridges[60].

X-ray photoelectron spectroscopy was performed to analyze the surface of the material synthesized. Survey spectrum of NdppzPMO (Fig. S5a) confirmed the presence of C, O, Si and N on the surface of the sample. The high C1s resolution spectrum was fitted into two components centered at 285.5 and 287.2 eV, which were associated to C-H/C-C/CAr and C=N, respectively (Fig. S5b). Concerning the N1s region (Fig. S5c), NdppzPMO showed a peak centered at 400.5 eV, which was attributed to the nitrogen atoms present on the dipyridyl-pyridazine units of NdppzPMO[55].

Formation of metal (Ru- and Ir-) complexes on the surface of NdppzPMO. The presence of dipyridylpyridazine units on NdppzPMO provides appropriate coordination sites for the formation of metal complexes on the PMO surface. Accordingly, two different metal complexes - Ru@NdppzPMO and Ir@NdppzPMO - were formed using NdppzPMO as ligand. For it, NdppzPMO was dispersed in an ethanol solution containing

the commercial metal precursor, $Ru(bpy)_2Cl_2 \cdot nH_2O$ and $[Ir(ppy)_2Cl]_2$, respectively (see Scheme 3).

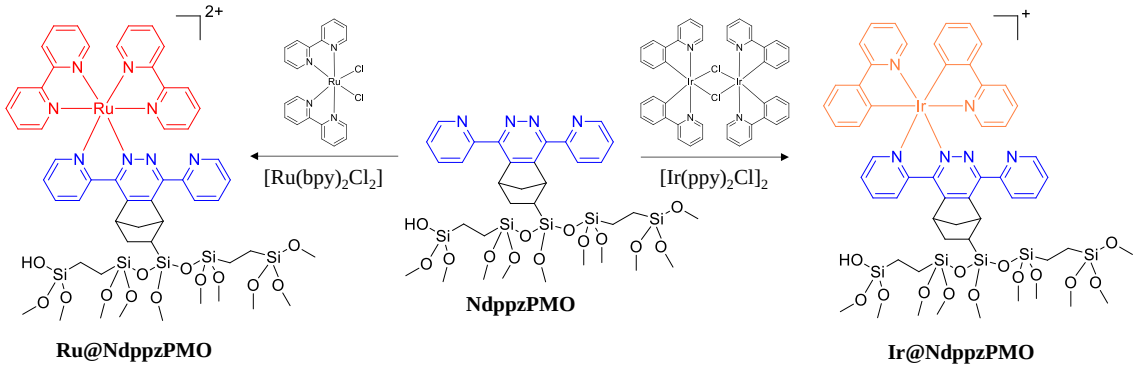

Scheme 3. Formation of Ru- and Ir- complexes using NdppzPMO as ligand.

The amount of metal precursors coordinated on the surface of the mesoporous support were determined by ICP-MS. The metal loadings were 0.14 mmol Ru g^{-1} for Ru@NdppzPMO and 0.12 mmol Ir g^{-1} for Ir@NdppzPMO, which corresponded to an 1.4 and 2.3 metal wt%, respectively. The nitrogen/metal ratio was below 4, which suggested the adsorption of a small amount of metal precursor on the surface of the NdppzPMO material and/or the formation of dinuclear complexes on the dipyridyl-pyridazine moieties. XRD patterns of metal functionalized PMO materials showed a strong reflection (100) at low angle 2θ, similar to the parent material (Fig. S6a and S7a), indicating that the initial ordered mesoporous structure was preserved after the formation of the surface metal complexes.

Fig. 2 shows conventional TEM images for both Ru@NdppzPMO and Ir@NdppzPMO samples. It should be noted that samples are sensitive to the electron beam and after a while can be damaged. Despite this fact, pore channels are clearly observed. Thus, pore channel size measurements were performed from TEM images with pore channel axis orientated parallel to the electron beam and increasing magnification. The equivalent planar diameters ($d = (4 \times \text{area}/\pi)^{1/2}$) obtained for Ru@NdppzPMO and Ir@NdppzPMO samples were 2.8 ± 0.2 nm and 3.2 ± 0.3 nm, respectively. These values are in good agreement with those obtained by DFT analysis, where 2.6 and 2.8 nm were estimated for Ru@NdppzPMO and Ir@NdppzPMO samples, respectively. Small differences could

be attributed to the fact that by TEM just a cross section is observed and analysed. However, DFT analysis provides values from the whole volume pore channels.

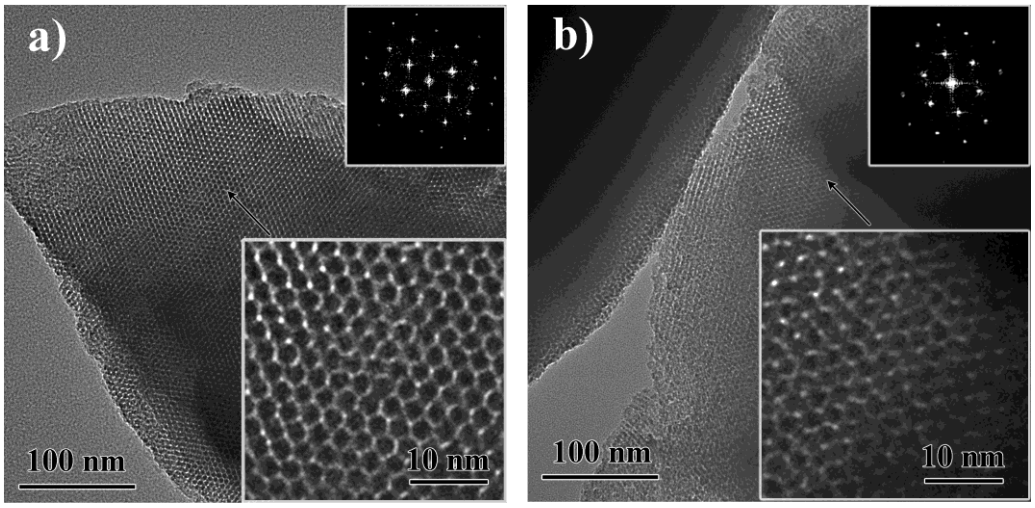

Fig. 2. Conventional TEM images for (a) Ru@NdppzPMO and (b) Ir@NdppzPMO. Both images contain a higher magnification inset and its corresponding FFT pattern.

Concerning the textural properties, both materials exhibited type-IV isotherms with a narrow pore size distribution (Fig. S6b and S7b). As can be clearly observed (Table 1), the formation of the metal complexes on the surface of NdppzPMO was accompanied by the decrease of BET surface area, pore volume and pore size, which was even more notable for Ru@NdppzPMO. However, a slight increase of the pore wall thickness (t) was observed for both materials, which might be ascribed to the volume occupied by the bipyridine and phenylpyridine groups coordinated to Ru^{+2} and Ir^{+3}, respectively[44]. Similar results were observed by our research group on the post-functionalization reactions over organosilica materials through Diels-Alder reaction with different dienes[52,54,57].

^{13}C CP/MAS NMR spectrum of Ru@NdppzPMO and Ir@NdppzPMO corroborated the formation of the metal complexes on the surface of NdppzPMO (Fig. 3). After coordination of ruthenium salt on the dipyridylpyridazine moieties, an increase of the aromatic resonances of the parent material was observed due to the presence of bipyridine ligands in the metal precursor. For Ir@NdppzPMO, additional signals at 144, 131 and 129-128 ppm were assigned to the aromatic rings of the phenylpyridine ligands[61].

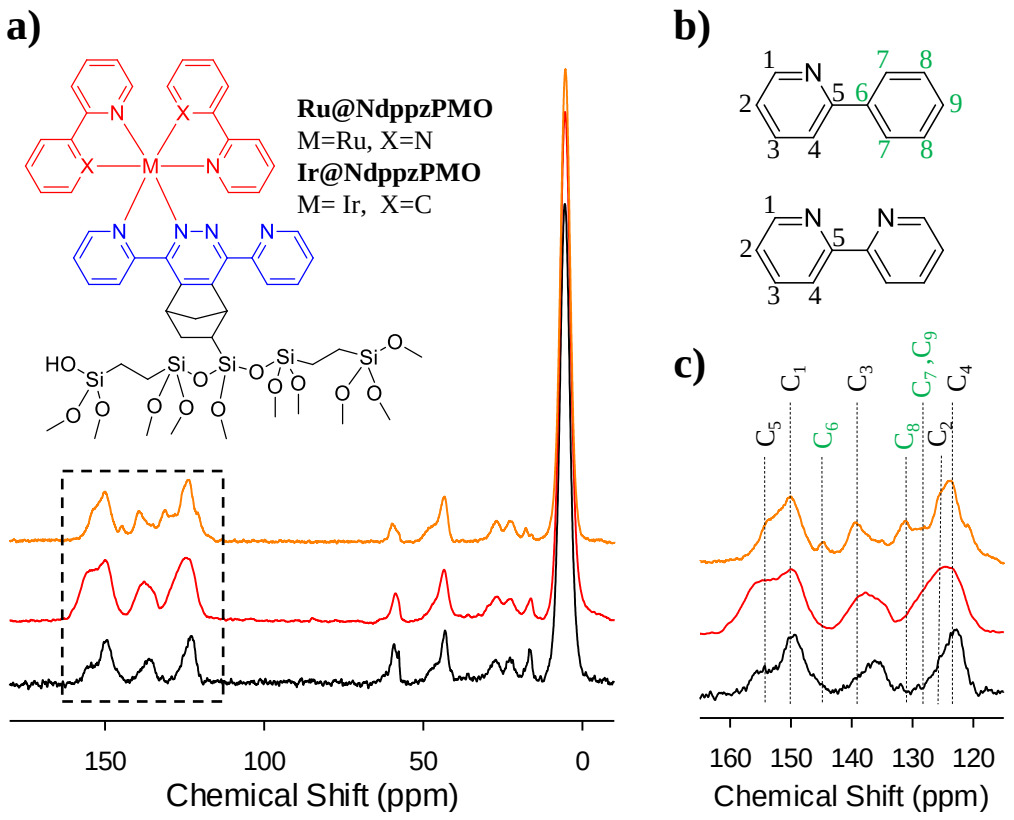

Fig. 3. (a) ^{13}C CP/MAS NMR spectrum of NdppzPMO (black solid line), Ru@NdppzPMO (red solid line) and Ir@NdppzPMO (orange solid line), (b) phenylpyridine and bipyridine ligand numbering and (c) aromatic carbons region and carbons assignments.

Additionally, the successful formation of metallic complexes on the surface of NdppzPMO can be further confirmed by optical spectroscopy. UV-Vis diffuse reflectance spectroscopy of Ru@NdppzPMO (Fig. 4a) revealed two broad adsorption bands at around 290 nm and 450 nm, which were assigned to $\pi \rightarrow \pi^*$ transtitions of bipyridine ligand and metal-to-ligand charge-transfer (MLCT), respectively[62,63]. Similar adsorption bands were shown for its homogeneous analogue $[Ru(bpy)_3]^{2+}$, and its metal precursor, $Ru(bpy)_2Cl_2 \cdot 2H_2O$. For this latter, a slight red-shifted MLCT band was observed at around 500 nm[64]. The spectrum of Ir@NdppzPMO (Fig. 4b) exhibited a wide band at around 390 nm attributed to MLCT transition. Additionally, this band was accompanied by an additional weak and long tail band above 450 nm corresponding to the direct spin-forbidden absorption from the singlet ground state to the triplet excited states, which is enabled by the high spin-orbit coupling constant of the iridium metal core.[65]

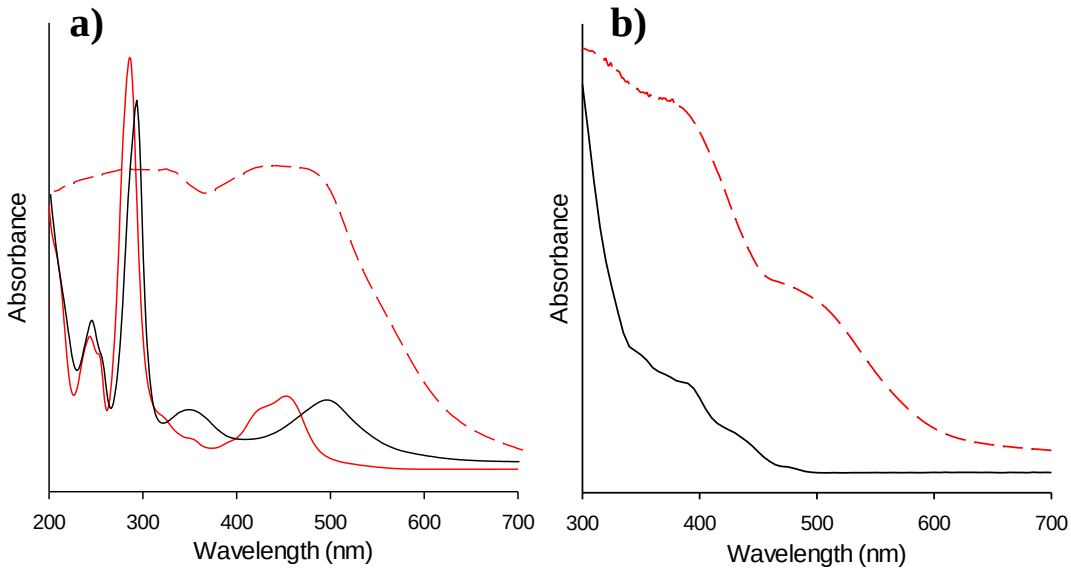

Fig. 4. (a) UV-vis absorption spectrum of $Ru(bpy)_2Cl_2 \cdot 2H_2O$ (black solid line) and $[Ru(bpy)_3]^{2+}$ (red solid line) in CH_3CN and UV-vis reflectance diffuse spectrum of Ru@NdppzPMO (red dashed line), (b) UV-vis absorption spectrum of $[Ir(ppy)_2Cl]_2$ (black line) in CH_2Cl_2 and UV-vis reflectance diffuse spectrum of Ir@NdppzPMO (red dashed line).

EDS mapping was performed in several regions to study the elemental distribution for Ru@NdppzPMO and Ir@NdppzPMO samples. Elemental EDS maps evidenced that Ru and Ir atoms were homogeneously distributed throughout the whole area (Fig. S8).

XPS measurements were performed to confirm the presence and oxidation state of complexed metallic species on the samples (Fig. 5). Survey spectrum of Ru@NdppzPMO and Ir@NdppzPMO confirmed the presence of C, Si, O, N on the samples, as previously observed for NdppzPMO, and additional peaks of Ru and Ir, respectively (Fig. S9). The C1s-Ru3d region for Ru@NdppzPMO showed two new peaks centered at 282.4 and 286.5 eV, compared to NdppzPMO, which were associated to the $Ru3d_{5/2}$ and $Ru3d_{3/2}$ spin-orbit components, respectively (Fig. 5a). These values of binding energies were in agreement with those reported in the literature for ruthenium in oxidation state +2[66–68]. Furthermore, the Ir4f spectrum for Ir@NdppzPMO showed a $Ir4f_{7/2}$ and $Ir4f_{5/2}$ doublet at 62.8 and 65.8 eV, respectively, suggesting the presence of Ir^{3+} in the sample (Fig. 5b)[69,70]. After coordination of ruthenium and iridium, no additional peaks could be deconvoluted regarding the C1s signals observed for NdppzPMO material confirming that the C1s

chemical environment remained unaltered after metal complexation (Fig. 5a and Fig. S10). In contrast, N1s XPS spectrum for Ru@NdppzPMO and Ir@NdppzPMO showed a slight shift of the peak maximum (400.5 eV) to higher binding energy (401.2 eV), which was ascribed to the electronic interaction between the metal and the nitrogen atoms of the dipyridylpyridazine units after complexation (Fig. S11)[71,72].

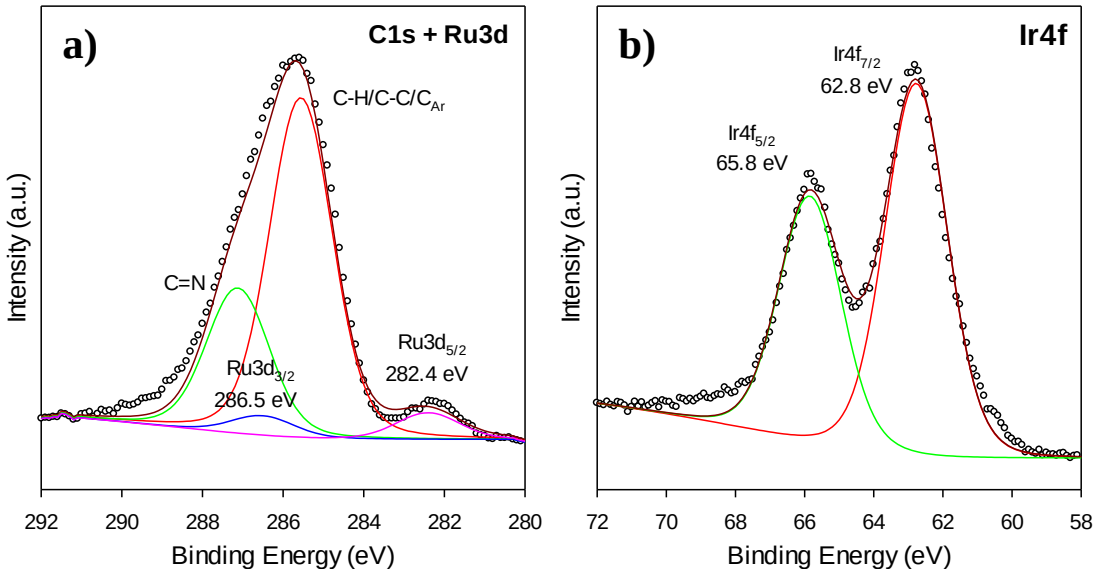

Fig. 5. (a) C1s and Ru3d XPS spectrum of Ru@NdppzPMO. (b) Ir4f XPS spectrum of Ir@NdppzPMO

Platinum supported on Ru- and Ir@NdppzPMO materials. Both Ru- and Ir-complexed PMO materials were employed as support for platinum species in their mesoporous framework walls. Thus, Ru@NdppzPMO and Ir@NdppzPMO were stirred in an aqueous solution containing the platinum precursor, K_2PtCl_6, without any subsequent treatment with reductant agent. ICP-MS measurements of both solids after Pt deposition showed a decrease in the amount of metal loading, particularly noteworthy in the case of the ruthenium complex. The amount of supported platinum was estimated as 0.35 mmol Pt·g^{-1} for Pt/Ru@NdppzPMO and 0.54 mmol·g^{-1} for Pt/Ir@NdppzPMO, corresponding to a metal/platinum ratio of 0.19 and 0.18, respectively.

XRD diffraction patterns of Pt/Ru@NdppzPMO and Pt/Ir@NdppzPMO (Fig. S12a and S13a) showed less intense diffraction peaks compared to their parent materials. In fact, d_{110} and d_{200} reflections at higher incidence angles were not observed. This could be caused by the reduction of scattering contrast produced by the dispersed metallic species inside the pore channels. Conversely, the presence of the d_{100} reflection for the Pt-

supported materials suggested the preservation of the ordered structure of the support, as further corroborated by TEM measurements (Fig. S12b and S13b). Moreover, pore channels have been clearly observed and measured, obtaining an equivalent planar diameter of 3.1 ± 0.4 nm and 3.4 ± 0.2 nm for Pt/Ru@NdppzPMO and Pt/Ir@NdppzPMO, respectively. These values were very similar to those obtained for metal functionalized PMO materials, so Pt deposition did not lead to a decrease in the ordering and had a negligible effect on the pore channel size. These results were in agreement with those reported in the literature for metal-supported mesoporous materials[73,74].

XPS measurements were collected to further confirm the deposition of Pt species on the solid supports (Fig. S14 and Fig. S15). Survey spectrum indicated the presence of Pt on the surface of both samples. The Pt4f XPS spectrum for Pt/Ru@NdppzPMO could be deconvoluted into a doublet pair centered at 77.2 and 73.9 eV, associated to $Pt4f_{5/2}$ and $Pt4f_{7/2}$, respectively (Fig. S1b). These peaks are assignable to tetravalent platinum[75]. Similar results were observed for Pt/Ir@NdppzPMO (Fig. S15b) with a $Pt4f_{5/2}$ and $Pt4f_{7/2}$ doublet at 77.9 and 74.6 eV, respectively.

Elemental mapping was carried out using energy dispersive X-ray spectroscopy (EDS) to study the elemental distribution for Pt/Ru@NdppzPMO and Pt/Ir@NdppzPMO samples (Fig. S16). Again, it is observed a homogenous distribution for Ru, Ir and Pt atoms throughout the sample. So, it seems that the presence of metal (Ru or Ir) in our functionalized PMO materials does not impede a good Pt distribution on the samples before reaction.

Evaluation of Pt/Ru@NdppzPMO and Pt/Ir@NdppzPMO as photocatalytic systems for H_2 production. The integration of the photosensitizer and catalytic units in a PMO is a highly attractive approach for solar energy conversion. To the best of our knowledge, only Inagaki and col. succeeded to synthesize an efficient photocatalytic HER system by integrating both Ru-complex and Pt as photosensitizer and catalyst, respectively, on the pore surface of a periodic mesoporous organosilica with 2,2'-bipyridine as bridging organic groups[44]. In this work, the potential of the photocatalytic systems - Pt/Ru@NdppzPMO and Pt/Ir@NdppzPMO – containing both photosensitizing and catalytic units was evaluated for light-driven hydrogen production in the presence of EDTA and MV^{+2} a sacrificial electron donor and an electron relay, respectively.

According to the literature[62,76,77], the proposed HER mechanism occurs as represented in Scheme 4: a) The photosensitizer acts as a light harvester and absorbs photons from visible light to reach an excited state (PS*); b) The PS* is oxidatively quenched by electron transfer from methyl viologen, MV^{2+}; c) The oxidized photosensitizer is reduced to its initial form by the sacrificial agent, which remains in an oxidized state; d) Finally, the reduced methyl viologen, MV^{+}, is reoxidised to MV^{2+} by transferring an electron to the catalyst, which decreases the energetic barrier for proton reduction promoting hydrogen evolution. It is reported that the electron relay is crucial in the electron transfer by quenching the excited state of the photosensitizer in a homogeneous system[78].

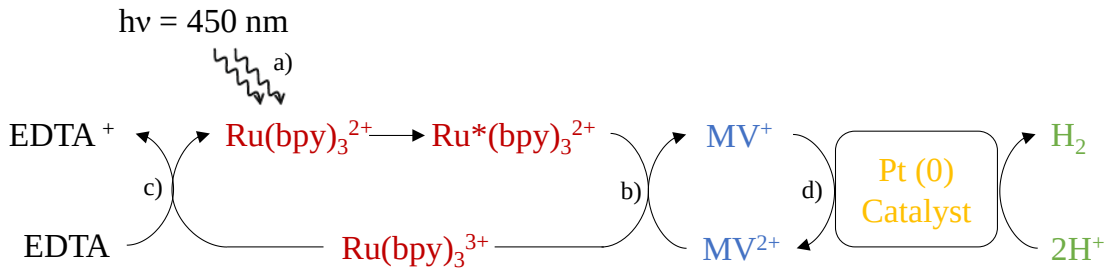

Scheme 4. Hydrogen evolution photocatalytic system composed of EDTA, $Ru(bpy)_3^{2+}$, MV^{2+}, and Pt catalyst under visible-light irradiation.

In our photocatalytic systems, efficient hydrogen production was observed when they were irradiated under visible light (450 nm) in an aqueous acetate buffer solution (pH= 5.0) containing EDTA as electron donor. Initially, a series of control reactions were carried out to confirm the role of all components on our photocatalytic system (Fig. S17). In absence of Pt (catalyst), the heterogeneous system containing Ru@NdppzPMO or Ir@NdppzPMO, MV^{+2} and EDTA as photosensitizer, electron relay and sacrificial electron donor, respectively, showed negligible hydrogen evolution. Similarly, a negligible amount of hydrogen was observed when Ru@NdppzPMO or Ir@NdppzPMO was replaced by an ethylene-bridged PMO without surface complexes, and K_2PtCl_6 as Pt source. Furthermore, the role of methyl viologen on HER was evaluated through two different approaches. First, control tests were performed using Ru@NdppzPMO or Ir@NdppzPMO and K_2PtCl_6. Under these conditions, a negligible hydrogen evolution was observed. Then, Pt/Ru@NdppzPMO or Pt/Ir@NdppzPMO were used instead of Ru@NdppzPMO or Ir@NdppzPMO, respectively, for having Pt species supported on the pore surface rather than in solution. These tests produced a slight amount of hydrogen

compared to the original three-component systems. This fact suggests that direct electron transfer could be possible between PS units and catalyst when the latter is supported on the pore surface due to the existence of Pt particles in close contact with Ru-/Ir-complexes. However, the small amount of PS units compared to Pt particles led to a considerable distance between both units within the photocatalytic system evidencing the need for an electron relay to carry out an efficient electron transfer between PS and the catalyst.

The H_2 evolving activities of Pt/Ru@NdppzPMO and Pt/Ir@NdppzPMO under the conditions previously mentioned are shown in Fig. 6. As can be observed, both photocatalytic systems (Figs 6a and c) showed an induction period before evolving hydrogen due to the required reduction of tetravalent platinum to the active platinum catalyst (Pt^0).[79,80] These results are in concordance with those previously obtained by XPS measurements, where the absence of Pt(0) was practically confirmed for both samples before irradiation. After such induction period, Pt/Ru@NdppzPMO produced hydrogen with an initial H_2 production rate of 1.50 mmol h^{-1} g^{-1}. The hydrogen production observed after 24 h was 19.9 μmol, which corresponded to 306 turnovers vs [Ru]. For Pt/Ir@NdppzPMO, although its activation period required longer times, the photosystem showed a faster production rate (2.08 mmol $h^{-1}\cdot g^{-1}$). The amount of evolved hydrogen in 24 h was 38.7 μmol with a turnover of 346 vs [Ir]. Long-time irradiation experiments were carried out to evaluate the lifetime of the Ru and Ir complexes anchored in the PMO (Fig. S18 and S19). Pt/Ru@NdppzPMO and Pt/Ir@NdppzPMO were irradiated for 120 and 168 h, respectively, until a plateau was reached in the kinetics profiles with a maximum hydrogen evolved amount of 37.3 and 94.8 μmol for Pt/Ru@NdppzPMO and Pt/Ir@NdppzPMO, respectively. Thus, a total turnover number (TTN) of 573 vs [Ru] was obtained for Pt/Ru@NdppzPMO while the TTN of Pt/Ir@NdppzPMO raised up to 846 vs [Ir]. These values clearly reflected the higher activity of Pt/Ir@NdppzPMO compared to its ruthenium counterpart. For comparison purposes only and taking into account that the catalytic systems are not completely identical, a TON of 184 after 24 h was reported by Inagaki and col.[44] using a bipyridine-bridged PMO as a solid chelating ligand for Ru complexes.

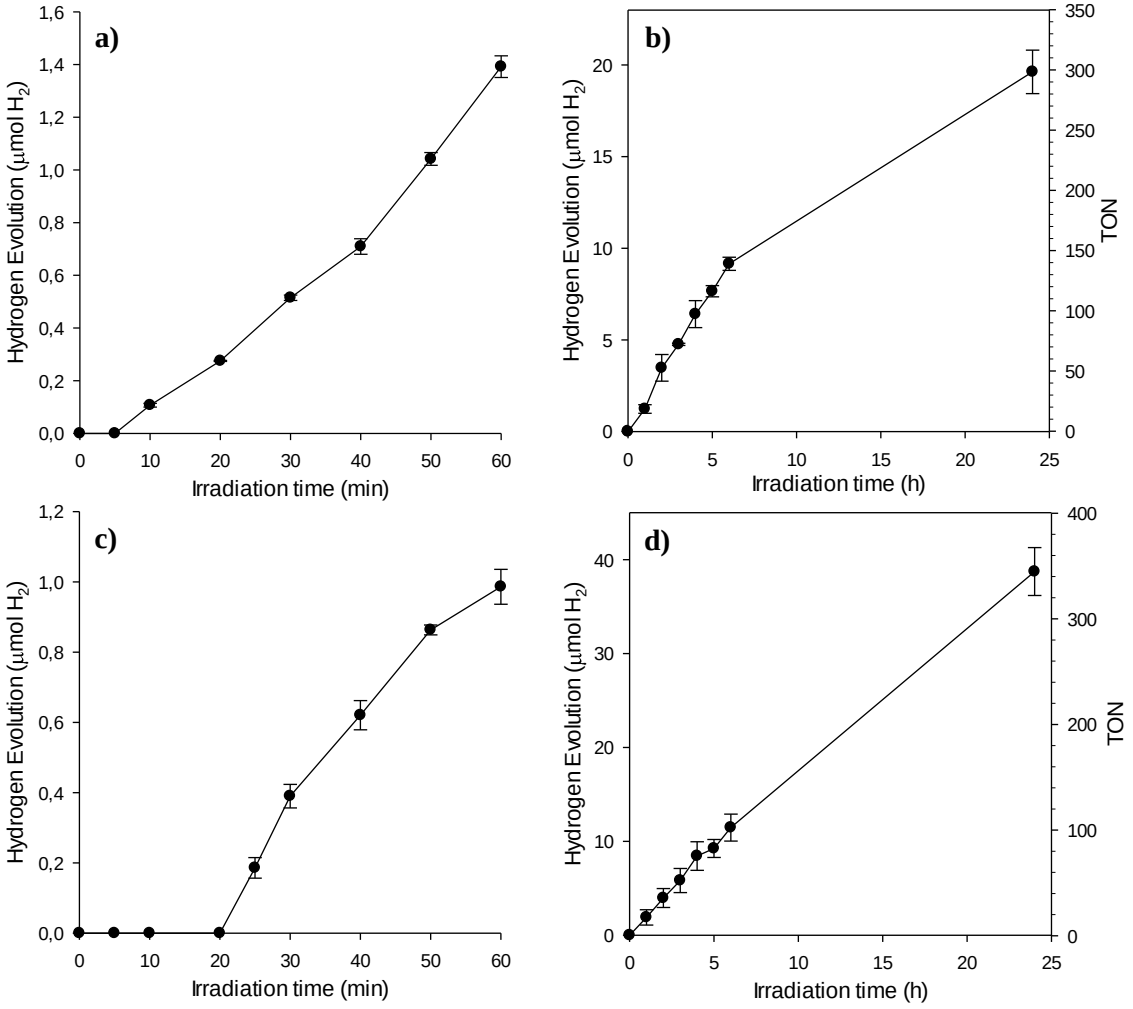

Fig. 6. Hydrogen evolution reaction at shorter reaction times with Pt/Ru@NdppzPMO (a) and Pt/Ir@NdppzPMO (c). Hydrogen evolution time dependence and turnover number of Pt/Ru@NdppzPMO (b) and Pt/Ir@NdppzPMO (d). Reaction conditions: 10 mL 1 M acetate buffer solution (pH 5.0), 1 mg catalyst, [EDTA]=20 mM, [MV]=5 mM. Light Source: $Led_{\lambda 450nm}$

Although $[Ru(bpy)_3]^{2+}$ possesses a strong absorption in the range of visible light with a maximum at 452 nm and a relatively long lifetime of the excited species, this type of complexes is characterized to exhibit low photostability due to its low-lying triplet metal centered (^{3}MC) excited state as well as its populated anti-bonding molecular orbital, which weakens the metal-ligand bond leading to degradation by ligand decoupling[81]. To offset ^{3}MC state limitation, cyclometalated Ir(III) complexes, such as $[Ir(ppy)_2(bpy)]^+$, exhibit greater ligand-field stabilization energy (LFSE) due to difference in σ-donation

ability between Ir-(C^N) bond and Ir-(N^N) bond, avoiding the population ^{3}MC of the dissociative state associated to $[Ru(bpy)_3]^{2+}$-based complexes. Thus, $[Ir(C^N)_2(N^N)]^+$ complexes exhibit higher stability and improved luminescence properties such as long excited-state lifetimes and tunable absorption wavelengths compared to tris-diimine Ru(II) complexes[82,83].

Additionally, leaching tests were performed to ensure that the H_2 production is produced heterogeneously by the active Pt species supported on the PMO photosystem and not by those leached from the material. For it, after 3 h of irradiation, the photocatalyst was removed from the solution and the supernatant was irradiated for additional 6 hours, showing negligible hydrogen evolution from the solution (Fig. S20).

Fig. S21 shows that the integrity of the ordered mesostructures was preserved in both Pt/Ru@NdppzPMO and Pt/Ir@NdppzPMO after irradiation for 24 h. Pore channels were observed, and size measurements provided an equivalent planar diameter of 3.2± 0.1 nm and 3.3 ± 0.2 nm for Pt/Ru@NdppzPMO and Pt/Ir@NdppzPMO, respectively. Again, these values were very close to those obtained before the irradiation process. So, it should be noted that Pt deposition and the subsequent irradiation treatment for 24 h did not influence channel size and they did not produce a loss of ordering in the mesostructure.

EDS mapping of these metal functionalized PMO materials after 24 h of irradiation showed the redistribution into particles experienced by Pt atoms, while Ru or Ir atoms were distributed throughout the full area (Fig. S22). The diameter of Pt particles was measured, obtaining an equivalent planar diameter value of 1.9 ± 0.1 nm. However, this Pt redistribution due to the irradiation process did not involve structural changes in the functionalized PMO materials, as was verified by TEM.

High resolution TEM images were taken from the Pt/Ru@NdppzPMO sample after 24 h of irradiation to study Pt particles. It was a challenging task since the sample was rather sensitive to the electron beam. As magnification was increasing and the beam focusing to the observing area, the sample was accumulating more and more damage and very often the area was destroyed before taking the image. Nevertheless, Fig. 7 was successfully taken. Noteworthy, although the mesostructure was fully disordered, several particles were observed, displaying lattice fringes inside. Fast Fourier Transform (FFT) of these particles are also shown. Reflection spots provide a d spacing of 0.23 nm, which is in very good agreement to the Pt (111) interplanar spacing value of 0.226 nm.

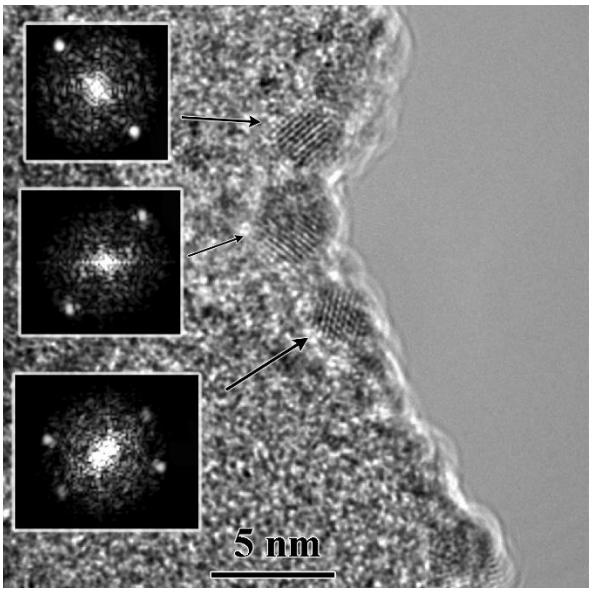

Fig. 7. High resolution TEM image for Pt/Ru@NdppzPMO after 24 h of irradiation. Several Pt particles are observed, whose FFT are shown.

After 24 h of irradiation of the photocatalysts under reaction conditions, XPS measurements of both samples (Fig. S14c and Fig. S15c) showed a new Pt4f doublet at lower binding energy than that reported for the material before irradiation, indicating the reduction of Pt(IV) to Pt(0). The valence change of the Pt species is associated with the formation of metallic Pt nanoparticles supported in the surface of the mesochannels[72,80].

While TEM images showed that the ordered mesostructures of these materials remained intact after 24 h of irradiation, ICP-MS measurements of both solids evidenced leaching of 57.0% Ru species and 36.4% Ir species into solution. In this sense, Tinker et al. reported the loss of the ^{3}MLCT excited state from the complex $[Ir(ppy)_2(bpy)]^+$ due to the cleavage of 2,2'-bipyridine moieties after irradiation with visible light[80], whereas a 20% photodegradation of the homogeneous $[Ru(bpy)_3]^{2+}$ complex after 4 h of irradiation is also reported in the literature[84]. Additionally, 54.3% and 42.6% of supported platinum in Pt/Ru@NdppzPMO and Pt/Ir@NdppzPMO, respectively, suffered leaching to solution after 24 h of reaction, which is in agreement with supported Pt NPs release under visible light irradiation[85,86].

The reusability of Pt/Ru@NdppzPMO and Pt/Ir@NdppzPMO for the hydrogen evolution reaction was evaluated after recovering both materials by filtration. As previously

discussed, after a first cycle of irradiation, photosensitizer complexes loading, and Pt supported species decreased significantly for both materials. As a result, hydrogen evolution decreased as the number of metal centers decreased. Despite the loss of photosensitizer and catalyst units, the PS/Pt ratio and the TON obtained with both systems remained stable (Fig. 8), indicating that Ru and Ir complexes coordinated to PMO exhibited similar light harvesting efficiency after 24 h of reaction.

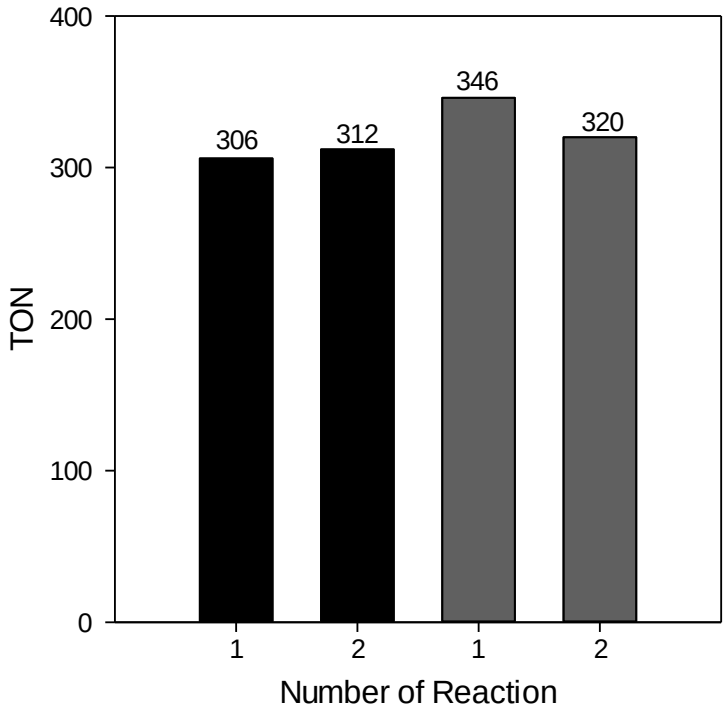

Fig. 8. Recycling experiments for Pt/Ru@NdppzPMO (black filled bar) and Pt/Ir@NdppzPMO (grey filled bar).

4. Conclusions

In summary, we reported the successfully synthesis of a novel dipyridilpyridazine based organosilane precursor through an iEDDA reaction between a norbornene organosilane and 3,6-di-(2-pyridyl)-1,2,4,5-tetrazine. This precursor was incorporated into the structure of a periodic mesoporous organosilica (NdppzPMO) affording a heterogeneous material with 2,2'-bipyridine-like units, which provides high coordination ability. The integration of Ru- and Ir-based complexes afforded two different photosensitizers, which,

in combination with supported Pt nanoparticles inside pore channels, acted as efficient heterogeneous photocatalysts in hydrogen evolution reaction.

The present strategy is very versatile since different tetrazines can be readily accessible from commercially available cyanopyridines and so different dipyridylpyridazine trialkoxysilanes could be synthesized analogously, thus giving rise to a new family organosilica precursors. Indeed, this approach provides an interesting and simple way to integrate different metal complexes in a variety of materials with potential applications as catalytic systems.

Conflicts of interest

There are no conflicts to declare.

Acknowledgements

The authors wish to acknowledge the financial support from Spanish Ministry of Science and Innovation for project RTI2018-101611-B-I00 and a FPI teaching and research fellowship (PRE2019-089122), Andalusian Regional Government (FQM-346 group) and Feder Funds. The technical staff from the Instituto Químico para la Energía y el Medioambiente (IQUEMA) and Servicio Central de Apoyo a la Investigación (SCAI) are also gratefully appreciated. M. C-R. thanks SCAI for allowing the TEM measurements.

References

1 A. Winter, G. R. Newkome and U. S. Schubert, *ChemCatChem*, 2011, **3**, 1384–1406.

2 R. Hoogenboom, G. Kickelbick and U. S. Schubert, *European J. Org. Chem.*, 2003, 4887–4896.

3 W. Kaim, *Coord. Chem. Rev.*, 2002, **230**, 127–139.

4 L. Saghatforoush, Z. Khoshtarkib, H. Keypour and M. Hakimi, *Polyhedron*, 2016, **119**, 160–174.

5 K. Parimal, E. H. Witlicki and A. H. Flood, *Angew. Chemie*, 2010, **122**, 4732–4736.

6 G. Li, K. Parimal, S. Vyas, C. M. Hadad, A. H. Flood and K. D. Glusac, *J. Am. Chem. Soc.*, 2009, **131**, 11656–11657.

7 W. Y. Yeh, G. H. Lee and S. M. Peng, *Inorganica Chim. Acta*, 2006, **359**, 659–664.

8 M. Maekawa, K. Sugimoto, T. Okubo, T. Kuroda-Sowa and M. Munakata, *Inorganica Chim. Acta*, 2017, **467**, 204–211.

9 M. Maekawa, T. Miyazaki, K. Sugimoto, T. Okubo, T. Kuroda-Sowa, M. Munakata and S. Kitagawa, *Dalt. Trans.*, 2013, **42**, 4258–4266.

10 B. L. Schottel, J. Bacsa and K. R. Dunbar, *Chem. Commun.*, 2005, **2**, 46–47.

11 E. C. Constable, C. E. Housecroft, M. Neuburger, S. Reymann and S. Schaffner, *CrystEngComm*, 2008, **10**, 991–995.

12 E. C. Constable, C. E. Housecroft, B. M. Kariuki, N. Kelly and C. B. Smith, *Inorg. Chem. Commun.*, 2002, **5**, 199–202.

13 H. Wu and N. K. Devaraj, *Acc. Chem. Res.*, 2018, **51**, 1249–1259.

14 J. Šečkute and N. K. Devaraj, *Curr. Opin. Chem. Biol.*, 2013, **17**, 761–767.

15 E. C. Constable, C. E. Housecroft, M. Neuburger, S. Reymann and S. Schaffner, *Chem. Commun.*, 2004, **4**, 1056–1057.

16 F. Thébault, A. J. Blake, C. Wilson, N. R. Champness and M. Schröder, *New J. Chem.*, 2006, **30**, 1498–1508.

17 F. Thalhammer, U. Wallfahrer and J. Sauer, *Tetrahedron Lett.*, 1990, **31**, 6851–6854.

18 M. L. Blackman, M. Royzen and J. M. Fox, *J. Am. Chem. Soc.*, 2008, **130**, 13518–13519.

19 F. Karaki, T. Kiguchi, K. Itoh, N. Sato, K. Konishi and H. Fujii, *Tetrahedron*, 2021, **97**, 132411.

20 H. C. Kolb, M. G. Finn and K. B. Sharpless, *Angew. Chemie - Int. Ed.*, 2001, **40**, 2004–2021.

21 F. Karaki, K. Ohgane, H. Imai, K. Itoh and H. Fujii, *European J. Org. Chem.*, 2017, 3815–3829.

22 N. Y. Kim, N. L. Jeon, I. S. Choi, S. Takami, Y. Harada, K. R. Finnie, G. S. Girolami, R. G. Nuzzo, G. M. Whitesides and P. E. Laibinis, *Macromolecules*, 2000, **33**, 2793–2795.

23 M. R. Giles and S. M. Howdle, *Eur. Polym. J.*, 2001, **37**, 1347–1351.

24 Y. Cai, J. Zheng and H. Fan, *Eur. Polym. J.*, 2022, **163**, 110941.

25 A. R. Bassindale, Z. Liu, I. A. MacKinnon, P. G. Taylor, Y. Yang, M. E. Light, P. N. Horton and M. B. Hursthouse, *J. Chem. Soc. Dalt. Trans.*, 2003, **3**, 2945–2949.

26 H. Acikalin, F. Ziegler, D. Wang and M. R. Buchmeiser, *Macromol. Chem. Phys.*, 2021, **222**, 1–5.

27 R. Bandari and M. R. Buchmeiser, *Catal. Sci. Technol.*, 2012, **2**, 220–226.

28 V. G. Bondaletov, A. A. Troyan, N. O. Kuhlenkova, M. V. Netesova, M. K. Zamanova and N. A. Baykova, *Procedia Chem.*, 2015, **15**, 259–264.

29 S. S. Kim, W. Zhang and T. J. Pinnavaia, *Catal. Letters*, 1997, **43**, 149–154.

30 Z. Luan, J. Xu and L. Kevan, *Chem. Mater.*, 1998, **10**, 3699–3706.

31 Y. X. Jiang, W. B. Song, Y. Liu, B. Wei, X. C. Cao and H. D. Xu, *Mater. Chem. Phys.*, 2000, **62**, 109–114.

32 K. Fujishima, A. Fukuoka, A. Yamagishi, S. Inagaki, Y. Fukushima and M. Ichikawa, *J. Mol. Catal. A Chem.*, 2001, **166**, 211–218.

33 Ogawa, M., T. Nakamura, J. I. Mori and K. Kuroda, *J. Phys. Chem. B*, 2000, **104**, 8554–8556.

34 J. V Nguyen and C. W. Jones, *Macromolecules*, 2004, **37**, 1190–1203.

35 C. D. Nunes, A. A. Valente, M. Pillinger, A. C. Fernandes and C. C. Roma, *J. Mater. Chem.*, 2002, **12**, 1735–1742.

36 L. Sun, W. Mai, S. Dang, Y. Qiu, W. Deng and L. Shi, *J. Mater. Chem.*, 2012, **22**, 5121–5127.

37 P. N. Minoofar, R. Hernandez, S. Chia, B. Dunn, J. I. Zink, A. Franville, V. Uni, B. Pascal, V. Landais and A. Cedex, *J. Am. Chem. Soc.*, 2002, **124**, 14388–14396.

38 J. Font, P. De March, E. Casas, M. Benitez and L. Teruel, *J. Mater. Chem.*, 2007, **17**, 2336–2343.

39 J. Corredor, M. J. Rivero, C. M. Rangel, F. Gloaguen and I. Ortiz, *J. Chem. Technol. Biotechnol.*, 2019, **94**, 3049–3063.

40 J. M. Lehn and J. P. Sauvage, *Nouv. J. Chim.*, 1977, **1**, 449–451.

41 O. S. Wenger, *Coord. Chem. Rev.*, 2009, **253**, 1439–1457.

42 C. C. Hou, T. T. Li, S. Cao, Y. Chen and W. F. Fu, *J. Mater. Chem. A*, 2015, **3**, 10386–10394.

43 C. Wang, E. Kathryn and W. Lin, *J. Am. Chem. Soc.*, 2012, **134**, 7211–7214.

44 M. Waki, Y. Maegawa, K. Hara, Y. Goto, S. Shirai, Y. Yamada, N. Mizoshita, T. Tani, W. J. Chun, S. Muratsugu, M. Tada, A. Fukuoka and S. Inagaki, *J. Am. Chem. Soc.*, 2014, **136**, 4003–4011.

45 G. H. Gunasekar, K. Park, H. Jeong, K. D. Jung, K. Park and S. Yoon, *Catalysts*, 2018, **8**, 1–16.

46 P. Van Der Voort, D. Esquivel, E. De Canck, F. Goethals, I. Van Driessche and S. S. Francisco Romero, *Chem. Soc. Rev.*, 2013, **42**, 3913–3955.

47 M. S. Robillard, H. M. Janssen, W. ten Houve and R. M. Versreegen, *US pat 9421274B2*, 2016.

48 A. Kaczmarek, D. Esquivel, J. Ouwehand, P. Van Der Voort, F. J. Romero-Salguero and R. Van Deun, *Dalt. Trans.*, 2017, **46**, 7878–7887.

49 M. Waki, N. Mizoshita, T. Tani and S. Inagaki, *Angew. Chemie - Int. Ed.*, 2011, **123**, 11871–11875.

50 R. A. Palmer and T. S. Piper, *Inorg. Chem.*, 1966, **5**, 864–878.

51 M. S. Lowry, W. R. Hudson, R. A. Pascal and S. Bernhard, *J. Am. Chem. Soc.*, 2004, **126**, 14129–14135.

52 M. Á. Navarro, J. Amaro-Gahete, J. R. Ruiz, C. Jiménez-Sanchidrián, F. J. Romero-Salguero and D. Esquivel, *Dalt. Trans.*, 2022, **51**, 4884–4897.

53 A. M. Kaczmarek, D. Esquivel, B. Laforce, L. Vincze, P. Van Der Voort, F. J. Romero-Salguero and R. Van Deun, *Luminescence*, 2018, **33**, 567–573.

54 D. Esquivel, A. M. Kaczmarek, C. Jiménez-Sanchidrián, R. Van Deun, F. J. Romero-

Salguero and P. Van der Voort, *J. Mater. Chem. C*, 2015, **3**, 2909–2917.

55 J. Amaro-Gahete, A. M. Kaczmarek, D. Esquivel, C. Jiménez-Sanchidrián, P. Van Der Voort and F. J. Romero-Salguero, *Chem. - A Eur. J.*, 2019, **25**, 6823–6830.

56 D. Esquivel, E. De Canck, C. Jiménez-Sanchidrián, P. Van Der Voort and F. J. Romero-Salguero, *J. Mater. Chem.*, 2011, **21**, 10990–10998.

57 D. Esquivel, E. De Canck, C. Jiménez-Sanchidrián, F. J. Romero-Salguero and P. Van Der Voort, *Mater. Chem. Phys.*, 2014, **148**, 403–410.

58 F. Hoffmann, M. Cornelius, J. Morell and M. Fröba, *Angew. Chemie - Int. Ed.*, 2006, **45**, 3216–3251.

59 M. I. López, D. Esquivel, C. Jiménez-Sanchidrián, F. J. Romero-Salguero and P. Van Der Voort, *J. Catal.*, 2015, **326**, 139–148.

60 M. Á. Navarro, D. Cosano, A. Bhunia, L. Simonelli, V. Martin-Diaconescu, F. J. Romero-Salguero and D. Esquivel, *Sustain. Energy Fuels*, 2022, **6**, 398–407.

61 L. Jian, H. Y. He, J. Huang, Q. H. Wu, M. L. Yuan, H. Y. Fu, X. L. Zheng, H. Chen and R. X. Li, *RSC Adv.*, 2017, **7**, 23515–23522.

62 K. Kalyanasundaram, *Coord. Chem. Rev.*, 1982, **46**, 159–244.

63 A. Juris, V. Balzani, F. Barigelletti, S. Campagna, P. L. Belser and A. von von Zelewsky, *Coord. Chem. Rev.*, 1988, **84**, 85–277.

64 D. M. Klassen and G. A. Crosby, *J. Chem. Phys.*, 1968, **48**, 1853–1858.

65 R. D. Costa, F. Monti, G. Accorsi, A. Barbieri, H. J. Bolink, E. Ortí and N. Armaroli, *Inorg. Chem.*, 2011, **50**, 7229–7238.

66 S. Tokarev, M. Rumyantseva, A. Nasriddinov, A. Gaskov, A. Moiseeva, Y. Fedorov and G. Jonusauskas, *Phys. Chem. Chem. Phys.*, 2020, **22**, 8146–8156.

67 A. Jana, J. Mondal, P. Borah, S. Mondal, A. Bhaumik and Y. Zhao, *Chem. Commun.*, 2015, **51**, 10746–10749.

68 C. Agnès, J. C. Arnault, F. Omnès, B. Jousselme, M. Billon, G. Bidan and P. Mailley, *Phys. Chem. Chem. Phys.*, 2009, **11**, 11647–11654.

69 A. V. Bavykina, M. G. Goesten, F. Kapteijn, M. Makkee and J. Gascon, *ChemSusChem*, 2015, **8**, 809–812.

70 S. De, L. Gevers, A. Emwas and J. Gascon, *ACS Sustain. Chem. Eng.*, 2019, **7**, 3933–3939.

71 M. Sajedi, Y. Mansoori, A. Nuri, D. Esquivel and M. Angeles Navarro, *ChemistrySelect*, 2021, **6**, 13060–13067.

72 P. Lei, M. Hedlund, R. Lomoth, H. Rensmo, O. Johansson and L. Hammarström, *J. Am. Chem. Soc.*, 2008, **130**, 26–27.

73 J. A. Wang, L. F. Chen, L. E. Noreña, J. Navarrete, M. E. Llanos, J. L. Contreras and O. Novaro, *Microporous Mesoporous Mater.*, 2008, **112**, 61–76.

74 C. Liu, R. Tan, N. Yu and D. Yin, *Microporous Mesoporous Mater.*, 2010, **131**, 162–169.

75 F. Şen and G. Gökağaç, *J. Phys. Chem. C*, 2007, **111**, 5715–5720.

76 J. Kiwi and M. Grätzel, 1979, **281**, 657–658.

77 M. Kirch, J. Lehn and J. Sauvage, 1979, **62**, 1345–1384.

78 E. Amouyal and B. Zidler, *Isr. J. Chem.*, 1982, **22**, 117–124.

79 P. N. Curtin, L. L. Tinker, C. M. Burgess, E. D. Cline and S. Bernhard, *Inorg. Chem.*, 2009, **48**, 10498–10506.

80 L. L. Tinker, N. D. Mcdaniel, P. N. Curtin, C. K. Smith, M. J. Ireland and S. Bernhard, *Chem. Eur. J.*, 2007, **13**, 8726–8732.

81 L. L. Tinker, N. D. Mcdaniel and S. Bernhard, *J. Mater. Chem.*, 2009, **19**, 3328–3337.

82 Y. Yuan, Z. Yu, D. Chen and Z. Zou, *Chem. Soc. Rev.*, 2016, **46**, 603–631.

83 A. R. Bevernaegie, S. A. M. Wehlin and B. Elias, *ChemPhotoChem*, 2021, **5**, 217–234.

84 K. Sakai and H. Ozawa, *Coord. Chem. Rev.*, 2007, **251**, 2753–2766.

85 M. Sun, C. Sun, X. Wang and Z. Su, *Catal. Commun.*, 2020, **137**, 105930.

86 J. Xiao, Q. Shang, Y. Xiong, Q. Zhang, Y. Luo, S. Yu and L. Jiang, *Angew. Chemie Int. Ed.*, 2016, **55**, 9389–9393.